Journal of Materials Chemistry A

PAPER

View Article Online
View Journal | View Issue



Cite this: J. Mater. Chem. A, 2019, 7, 19348

# Asymmetric A–D–π–A-type nonfullerene small molecule acceptors for efficient organic solar cells†

Xueshan Li,‡[a] Chao Li,‡[a] Linglong Ye,[a] Kangkang Weng,[a] Huiting Fu,[a] Hwa Sook Ryu,[b] Donghui Wei,[c] Xiaobo Sun,*[a] Han Young Woo[b] and Yanming Sun*[a]

Received 17th June 2019
Accepted 29th July 2019

DOI: 10.1039/c9ta06476a

rsc.li/materials-a

There has been significant progress with regard to research on nonfullerene small molecule acceptors (SMAs) during the past several years. Typically, high-performance nonfullerene SMAs are based on symmetric A–D–A or A–π–D–π–A structural frameworks. In this study, a novel asymmetric nonfullerene SMA, TTPT-T-2F, with an A–D–π–A structure is rationally designed and synthesized. In addition, a symmetric A–D–A-type nonfullerene SMA, IT-2F, and a symmetric A–π–D–π–A-type nonfullerene SMA, T-TPT-T-2F, are also synthesized for comparison. When PBT1-C is employed as a polymer donor, a promising power conversion efficiency (PCE) of 12.71% is achieved for TTPT-T-2F-based organic solar cells (OSCs), which surpasses those of devices based on IT-2F (PCE = 10.54%) and T-TPT-T-2F (PCE = 10.71%). Favorable phase separation toward efficient and more balanced charge transport accounts for the higher PCE achieved in the PBT1-C:TTPT-T-2F device. Our results demonstrate that a small molecule acceptor with an A–D–π–A structural framework is a promising class of nonfullerene acceptors for OSCs.



## Introduction

Organic solar cells (OSCs) have attracted considerable research interest because of their distinct advantages, including low manufacturing cost, light weight, semi-transparency, and mechanical flexibility.[1–4] In the past decades, fullerene derivatives have been the dominant electron acceptors in OSCs.[5–7] Nevertheless, the intrinsic drawbacks of fullerenes such as weak absorption in the visible spectral region, difficulty in chemical modification, and poor thermal stability impede the further development of OSCs.[8,9] Therefore, in recent years, considerable effort has been focused on designing nonfullerene small molecule acceptors (SMAs), which can address these disadvantages of fullerene derivatives.[10–12] To date, state-of-the-art OSCs based on nonfullerene SMAs have achieved power conversion efficiencies (PCEs) of over 15%,[13,14] thus greatly outperforming fullerene-based devices.

Among the various nonfullerene SMAs, nonfullerene SMAs with acceptor–donor–acceptor (A–D–A) configurations have been widely studied in OSCs.[15] Typically, A–D–A-type nonfullerene SMAs have three components: an electron-donating fused-ring core (D), an electron-accepting terminal (A), and outstretched side chains. Through chemical modification of the central D unit,[16–21] side chain,[22–24] and/or terminal A unit,[25–30] numerous A–D–A-type nonfullerene SMAs have been reported. In addition, several research groups have explored the insertion of aromatic π-bridging units between D and A units in A–D–A-type nonfullerene SMAs (A–π–D–π–A) to tune the electronic and optical properties. For example, Bo *et al.* used alkoxy-substituted benzene as a π-bridging unit to synthesize an A–π–D–π-A-type nonfullerene SMA, IDT-BOC6, in which non-covalent intramolecular interaction was introduced to improve the PCE.[31] Hou *et al.* reported an A–π–D–π–A-type nonfullerene SMA, IEICO-4F, with an ultra-narrow optical bandgap by introducing two π-bridging alkoxy-substituted thiophene units.[32] Zhu *et al.* reported an A–π–D–π–A-type nonfullerene SMA, ATT-2, with thieno[3,4-*b*]thiophene bearing a quinoidal structure as the π-bridging unit, which showed a PCE of 9.58% in OSCs with PTB7-Th as the polymer donor.[33] These results suggest that introducing aromatic π-bridging units into A–D–A-type nonfullerene SMAs is an effective strategy to modify the optical and electronic properties of nonfullerene SMAs. Recent research has indicated that some asymmetric A–D–A-type nonfullerene SMAs can achieve better photovoltaic performance than the corresponding symmetric A–D–A-type nonfullerene SMAs.[34–36]

Inspired by the aforementioned results, we first report a novel asymmetric A–D–π–A-type nonfullerene SMA (NFA). As shown in Fig. 1, when a molecular cutting strategy is used to

[a]School of Chemistry, Beihang University, Beijing 100191, China. E-mail: sunxb@buaa.edu.cn; sunym@buaa.edu.cn

[b]Department of Chemistry, College of Science, Korea University, Seoul 136-713, Republic of Korea

[c]The College of Chemistry and Molecular Engineering, Zhengzhou University, Zhengzhou, Henan Province 450001, China

† Electronic supplementary information (ESI) available. See DOI: 10.1039/c9ta06476a

‡ These two authors contributed equally to this work.

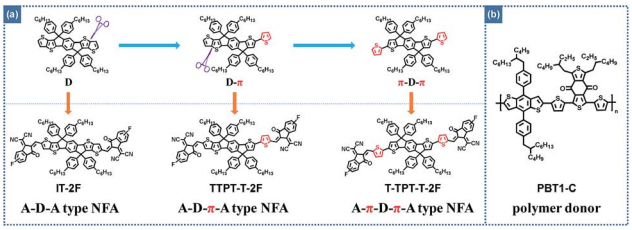


Fig. 1 (a) Molecular design strategy and chemical structures of IT-2F, TTPT-T-2F, and T-TPT-T-2F and (b) the chemical structure of PBT1-C.

remove one thiophene unit from the outside thieno[3,2-*b*]thiophene in an indacenodithienothiophene (IDTT) skeleton,[37] an asymmetric TPTT[35] derivative (TTPT-T) with a D–π structure can be developed as an analog of IDTT. Then, another thiophene unit is removed from the thieno[3,2-*b*]thiophene in the TPTT derivative, which leads to a symmetric indacenodithiophene (IDT) derivative (T-TPT-T) with a π–D–π structure. These three building blocks have the same numbers of aromatic rings but have different conjugated fused-ring structures. We then design and synthesize an A–D–π–A-type asymmetric nonfullerene SMA, TTPT-T-2F, with an asymmetric TTPT unit as the central electron-donating core as well as a monofluorinated 1,1-dicyanomethylene-3-indanone (IC) group as terminal electron-accepting unit and a thiophene as a π-bridging unit. For comparison, the A–D–A-type symmetric nonfullerene SMA IT-2F with a fully fused-ring core and the A–π–D–π–A-type symmetric nonfullerene SMA T-TPT-T-2F with a lower fused-ring core and two π-bridging units are also synthesized. From IT-2F to TTPT-T-2F and then to T-TPT-T-2F, the decreased fused-ring structure and increased π-bridging units result in red-shifting absorption spectra, elevating molecular energy levels, improving electron mobility and increasing intermolecular π–π stacking. When PBT1-C is used as the donor,[38] OSCs based on IT-2F, TTPT-T-2F, and T-TPT-T-2F yield PCEs of 10.54%, 12.71%, and 10.71%, respectively. The efficient and more balanced charge transport in the blend film contributed to the achieved high PCE in PBT1-C:TTPT-T-2F devices. These results demonstrate that A–D–π–A-type nonfullerene SMAs can represent a brand-new class of nonfullerene SMAs for the fabrication of high-efficiency OSCs.

## Results and discussion

The chemical structures of IT-2F, TTPT-T-2F, and T-TPT-T-2F are shown in Fig. 1a. IT-2F was synthesized according to the reported literature.[39] The synthetic routes of TTPT-T-2F and T-TPT-T-2F are illustrated in Scheme S1,† and detailed experimental procedures are presented in the ESI.† For the synthesis of TTPT-T-2F, compound **1** was reacted with [2,2′-bithiophen]-5-yltributylstannane through a Stille coupling reaction to obtain compound **2**. Subsequently, compound **2** was subjected to double nucleophilic addition with 4-hexylbenzene magnesium bromide to produce two benzyl alcohols, which was followed by an intramolecular Friedel–Crafts reaction to obtain an asymmetric building block, TTPT-T. Then, two formyl groups were introduced into TTPT-T to produce TTPT-T-CHO, which was followed by a Knoevenagel condensation reaction with monofluorinated IC end-capping groups to produce the final target TTPT-T-2F. Similar synthetic routes were used to obtain T-TPT-T-2F. These three nonfullerene SMAs all showed excellent solubility in common organic solvents such as chloroform and chlorobenzene at room temperature, thus ensuring efficient formation of a spin-coated film through solution processing.

Density functional theory (DFT) calculations were performed to understand the geometric conformations and electron distributions of frontier molecule orbitals of the three nonfullerene SMAs at the B3LYP/6-31G (d, p) level. As shown in Fig. S1,† the optimized molecular backbones of the three nonfullerene SMAs all exhibited nearly planar conformations, which should be beneficial for charge transport. For all structures, the highest occupied molecular orbital (HOMO) was mainly localized on the central donor unit, whereas the lowest unoccupied molecular orbital (LUMO) was delocalized along the entire conjugated backbone. However, the distribution properties of LUMOs over terminal groups were different for the three nonfullerene SMAs. The delocalization degrees of the LUMO over the terminal groups followed the order of IT-2F > TTPT-T-2F > T-TPT-T-2F. In addition, the HOMO/LUMO energy levels were determined to be −5.55/−3.43 eV for IT-2F, −5.46/−3.40 eV for TTPT-T-2F, and −5.37/−3.39 eV for T-TPT-T-2F.

UV-Vis absorption measurements were conducted to investigate the photo-physical properties of the three nonfullerene SMAs. The normalized absorption spectra of the three nonfullerene SMAs in diluted chlorobenzene solution and thin films are depicted in Fig. 2. All molecules showed similar absorption profiles both in solution and thin films. With the increase in the number of π-bridging units in the three nonfullerene SMAs, the maximum absorption peaks and the absorption spectra in total were all gradually red-shifted, which may derive from the fact that the emergence of thiophene π-bridging units could efficiently extend the conjugation length

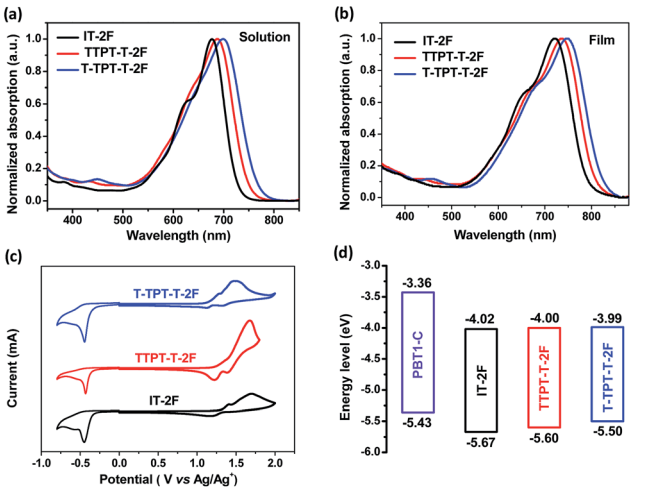


Fig. 2 Absorption spectra of the three nonfullerene SMAs (a) in diluted chlorobenzene solution and (b) in films; (c) cyclic voltammograms of the three nonfullerene SMAs; (d) energy level diagram of PBT1-C and the three nonfullerene SMAs.

and thus lead to bathochromic behavior.[40] IT-2F, TTPT-T-2F, and T-TPT-T-2F exhibited absorption peaks at 677, 688, and 700 nm in solution, and 720, 737 and 749 nm in films, respectively. From solution to film, the three nonfullerene SMAs showed broader absorption spectra and all the maximum absorption peaks displayed a distinct red-shift, suggesting the existence of strong intermolecular interactions in the solid state for the three nonfullerene SMAs.[41] The film onset absorption wavelengths of IT-2F, TTPT-T-2F, and T-TPT-T-2F were 789, 805, and 822 nm, which corresponded to the optical bandgaps of 1.57, 1.54, and 1.51 eV, respectively. Cyclic voltammetry measurements were employed to investigate the electrochemical properties of the three nonfullerene SMAs. As depicted in Fig. 2c, the onset oxidation/reduction potentials of IT-2F, TTPT-T-2F, and T-TPT-T-2F relative to Ag/AgCl were measured to be 1.31/−0.34, 1.24/−0.36, and 1.14/−0.37 V, respectively. Regarding the external standard ferrocene, it showed an onset oxidation potential of 0.44 V. Therefore, the corresponding HOMO/LUMO energy levels of IT-2F, TTPT-T-2F, and T-TPT-T-2F were estimated to be −5.67/−4.02, −5.60/−4.00, and −5.50/−3.99 eV, respectively, agreeing well with the variation trend of DFT calculations. The fact that HOMOs and LUMOs gradually increased from IT-2F to TTPT-T-2F and then to T-TPT-T-2F with an increase in the number of thiophene π-bridges indicates that introducing the proper number of π-bridges is a feasible and effective strategy to precisely manipulate the frontier orbital energy levels of nonfullerene SMAs. The corresponding optical and electrochemical data are summarized in Table 1.

To evaluate their photovoltaic performances, OSCs with an inverted structure of ITO/ZnO/active layer/$MoO_3$/Ag were fabricated. A wide-bandgap polymer donor PBT1-C (Fig. 1b) was employed as the donor because PBT1-C possesses a complementary absorption range with the three nonfullerene SMAs. The active layer morphology was systematically optimized as a function of various processing conditions including donor/acceptor ratios, the content of the DIO additive, and thermal annealing temperatures. The detailed device results are presented in Fig. S2–S4 and Table S1–S3.† The *J*–*V* curves and corresponding photovoltaic data of the optimized devices are depicted in Fig. 3a and Table 2. TTPT-T-2F-based devices had the highest PCE of 12.71% with an open-circuit voltage ($V_{oc}$) of 0.915 V, a short-circuit current density ($J_{sc}$) of 18.50 mA cm$^{-2}$, and a fill factor (FF) of 75.1% under the optimal conditions of a donor/acceptor (D/A) ratio of 1 : 1.5, DIO additive at 0.5% by volume and 100 °C thermal annealing (TA) temperature. Under the optimal conditions of a D/A ratio of 1 : 1, no additives and

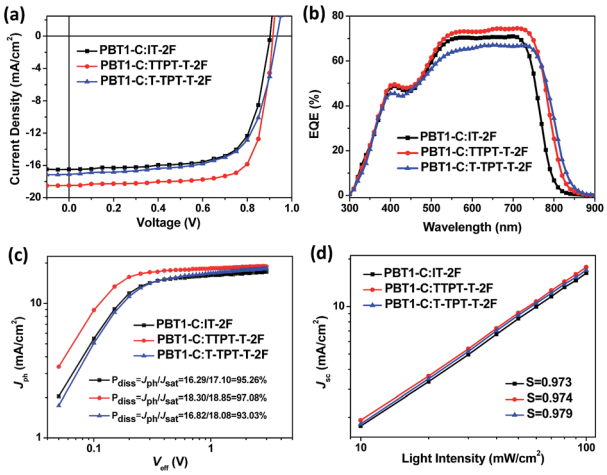


Fig. 3 (a) *J*–*V* curves and (b) EQE curves of the optimized devices based on the three nonfullerene SMAs. The evolution of (c) $J_{ph}$ *versus* $V_{eff}$ and (d) $J_{sc}$ *versus* light intensity (*P*).

130 °C TA temperature, IT-2F-based devices displayed a PCE of 10.54% along with a $V_{oc}$ of 0.902 V, a $J_{sc}$ of 16.50 mA cm$^{-2}$, and a FF of 70.8%, whereas T-TPT-T-2F-based devices showed a PCE of 10.71% with a $V_{oc}$ of 0.933 V, a $J_{sc}$ of 17.10 mA cm$^{-2}$, and a FF of 67.1%. The superior photovoltaic performances mainly originating from the high $J_{sc}$ and FF values for TTPT-T-2F-based OSCs demonstrated the rational feasibility for application of A–D–π–A-type asymmetric nonfullerene SMAs in the field of OSCs. Intriguingly, PCEs and other photovoltaic parameters of devices based on PBT1-C:IT-2F and PBT1-C:T-TPT-T-2F significantly decreased with the addition of DIO, which might be related to the formation of unfavorable morphology induced by the function of additives.[42,43] Thus, the optimal conditions for IT-2F-based and T-TPT-T-2F-based devices were at the D : A ratio of 1 : 1 with thermal treatment at 130 °C. The thermal stability of the devices was tested by heating the blend films under the optimal conditions at 100 °C. After continuous heating for 480 min, the PCEs and the other photovoltaic parameters of the three devices did not exhibit a decreasing trend (Fig. S5†), indicating that all the active layers possess excellent morphological stability. The variation trend of $V_{oc}$ for the three nonfullerene SMA-based OSCs was consistent with their LUMO levels, as the value of $V_{oc}$ in OSCs is related to the offset of the HOMO of the donor and LUMO of the acceptor.[44–46]

The corresponding external quantum efficiency (EQE) curves of the three nonfullerene SMA-based devices are displayed in Fig. 3b. The onset wavelengths for photo-responses of the three

Table 1 Optical and electrochemical properties of the three NFAs

| NFA | $\lambda_{max}{}^a$ [nm] | $\lambda_{max}{}^b$ [nm] | $\lambda_{onset}{}^b$ [nm] | $E_g^{optc}$ [eV] | $E_{ox}$ [V] | HOMO [eV] | $E_{red}$ [V] | LUMO [eV] |
|---|---|---|---|---|---|---|---|---|
| IT-2F | 677 | 720 | 789 | 1.57 | 1.31 | −5.67 | −0.34 | −4.02 |
| TPTT-T-2F | 688 | 737 | 805 | 1.54 | 1.24 | −5.60 | −0.36 | −4.00 |
| T-TPT-T-2F | 700 | 749 | 822 | 1.51 | 1.14 | −5.50 | −0.37 | −3.99 |

[a] In chlorobenzene solution. [b] In a thin film drop cast from the chlorobenzene solution. [c] Estimated using the empirical formula: $E_g^{opt} = 1240/\lambda_{onset}$.

Table 2 Photovoltaic parameters of the three nonfullerene SMA-based devices under optimal conditions

| NFA | $V_{oc}$ (V) | $J_{sc}$ (mA cm$^{-2}$) | $J_{sc,cal}$ (mA cm$^{-2}$) | FF (%) | PCE[a] (%) |
|---|---|---|---|---|---|
| IT-2F | 0.902 (0.897 ± 0.006) | 16.50 (16.23 ± 0.17) | 15.97 | 70.8 (69.6 ± 1.3) | 10.54 (10.13 ± 0.33) |
| TTPT-T-2F | 0.915 (0.910 ± 0.004) | 18.50 (18.32 ± 0.14) | 17.70 | 75.1 (75.0 ± 0.6) | 12.71 (12.51 ± 0.14) |
| T-TPT-T-2F | 0.933 (0.931 ± 0.001) | 17.63 (17.21 ± 0.17) | 16.57 | 67.1 (66.0 ± 1.0) | 10.71 (10.58 ± 0.09) |

[a] Average values with standard deviations were obtained from 20 devices.

curves increase in the order of PBT1-C:T-TPT-T-2F > PBT1-C:TTPT-T-2F > PBT1-C:IT-2F, which is consistent with the variation trend of onset wavelengths of absorption for the three nonfullerene SMAs. Of the three nonfullerene SMA-based devices, TTPT-T-2F-based devices exhibited the best photo-response with a maximum EQE approaching 75% at ~710 nm and a high EQE over 70% in the range of 540–740 nm, thus obtaining the highest integrated current of 17.70 mA cm$^{-2}$. By contrast, the maximum EQE values for IT-2F-based and T-TPT-T-2F-based devices were 70.93% at ~710 nm and 67.03% at ~650 nm, respectively. Although the T-TPT-T-2F-based devices exhibited the lowest EQE across the entire overlapping photo-response ranges of the three nonfullerene SMA-based devices, the broadest EQE range contributed to its higher integrated current of 16.57 mA cm$^{-2}$ as compared to that (15.97 mA cm$^{-2}$) of IT-2F-based devices with modest photo-response and medial EQE values. These integrated current values were consistent with device measurement values within a mismatch of 5%.

Space charge limited current (SCLC) measurements were employed to estimate the hole and electron mobility of the three nonfullerene SMAs and their blend films to study the charge transport properties of the optimized devices. The corresponding detailed data are presented in Fig. S6 and Table S4.† For the pristine NFA films, from IT-2F to TTPT-T-2F and then to T-TPT-T-2F, the average electron mobilities ($\mu_e$) gradually increased and the corresponding $\mu_e$ values were measured to be $3.26 \times 10^{-4}$, $6.59 \times 10^{-4}$, and $7.72 \times 10^{-4}$ cm$^2$ V$^{-1}$ s$^{-1}$, respectively. However, for the blend films, the $\mu_e$ values of PBT1-C:IT-2F, PBT1-C:TTPT-T-2F, and PBT1-C:T-TPT-T-2F were reduced to $1.89 \times 10^{-4}$, $3.55 \times 10^{-4}$, and $1.16 \times 10^{-4}$ cm$^2$ V$^{-1}$ s$^{-1}$, respectively. We speculated that the lower $\mu_e$ of PBT1-C:IT-2F and PBT1-C:T-TPT-T-2F compared to that of PBT1-C:TTPT-T-2F may be relevant to the different miscibility and resulting blend morphology of the three nonfullerene SMAs with the donor PBT1-C. Therefore, we carried out contact angle measurements (Table S5†) by using liquid drops of water ($\theta_{water}$) and glycerol ($\theta_{Gl}$), and the surface energies ($\gamma$) were calculated using the Wu model.[47] As shown in Table 3, the surface energies of IT-2F, TTPT-T-2F and T-TPT-T-2F were 27.8, 25.8, and 27.4 mJ m$^{-2}$, respectively. With respect to the donor material, PBT1-C possesses a surface energy of 27.2 mJ m$^{-2}$. The surface energy differences ($\Delta\gamma$) between IT-2F, TTPT-T-2F, and T-TPT-T-2F NFAs and the PBT1-C donor were 0.6, 1.4, and 0.2 mJ m$^{-2}$, respectively. The higher $\Delta\gamma$ values of TTPT-T-2F than of IT-2F and T-TPT-T-2F when blended with PBT1-C may induce lower miscibility, which probably suggested a higher domain purity and thus benefited the formation of excellent charge transport channels, finally leading to the higher $\mu_e$ value for the TTPT-T-2F-based blend. Hence, the blend film based on PBT1-C:TTPT-T-2F exhibited the highest hole ($\mu_h = 1.18 \times 10^{-3}$ cm$^2$ V$^{-1}$ s$^{-1}$) and electron mobility as well as the most balanced ($\mu_h/\mu_e = 3.32$) charge transport, which are beneficial to reducing bimolecular recombination and facilitating charge transport to the corresponding electrodes. This is also consistent with the highest FF values obtained in the corresponding OSCs.

The dependence of photocurrent density ($J_{ph}$) on effective voltage ($V_{eff}$) was measured to investigate photon harvesting and exciton dissociation characteristics. The $J_{ph}$ is defined as $J_{ph} = J_L - J_D$, where $J_L$ and $J_D$ represent the circuit density under illumination and dark conditions, respectively. In addition, the $V_{eff}$ is defined as $V_{eff} = V_0 - V_{bias}$, where $V_0$ is the voltage at which $J_{ph}$ is zero and $V_{bias}$ is the external bias voltage.[48] Mobile charge carriers move rapidly toward the corresponding electrodes with minimum recombination at a sufficiently high effective voltage, resulting in the formation of a saturated photocurrent density ($J_{sat}$). As shown in Fig. 3c, all the three nonfullerene SMA-based devices reached the $J_{sat}$ at $V_{eff} \geq 2$ V, indicating that the excitons dissociated efficiently into mobile charge carriers and were collected by electrodes. The $J_{sat}$ values of IT-2F-, TTPT-T-2F-, and T-TPT-T-2F-based devices were measured to be 17.10, 18.85, and 18.08 mA cm$^{-2}$, respectively, which suggests that TTPT-T-2F-based OSCs have the strongest photo-harvesting capabilities. The exciton dissociation probabilities ($P_{diss}$) could be calculated from the $J_{ph}$ under short-circuit conditions divided by the $J_{sat}$. Therefore, the $P_{diss}$ values for IT-2F-, TTPT-T-2F-, and T-TPT-T-2F-based OSCs were calculated to be 95.26%, 97.08%, and 93.03%, respectively. Thus, the fact that TTPT-T-based OSCs had the highest $P_{diss}$ in contrast to the other two nonfullerene SMA-based OSCs could lead to obtaining the highest $J_{sc}$.

Table 3 Contact angles of nonfullerene SMAs and PBT1-C and their corresponding surface energies

| Materials | $\theta_{water}$ (°) | $\theta_{Gl}$ (°) | $\gamma$ (mJ cm$^{-2}$) | $\Delta\gamma$[a] (mJ cm$^{-2}$) |
|---|---|---|---|---|
| IT-2F | 95.95 | 79.91 | 27.8 | 0.6 |
| TTPT-T-2F | 94.74 | 81.58 | 25.8 | 1.4 |
| T-TPT-T-2F | 95.32 | 79.91 | 27.4 | 0.2 |
| PBT1-C | 100.51 | 83.31 | 27.2 | |

[a] The surface energy differences between NFAs and PBT1-C.

To investigate the behavior of charge separation and recombination, the evolutionary trend of $J_{sc}$ *versus* light intensity ($P$) was measured. The relationship between the $J_{sc}$ and $P$ obeys the following exponential relation: $J_{sc} \propto P^{\alpha}$, where $\alpha$ denotes the degree of bimolecular recombination. Under given circumstances, if all the carriers dissociated by photogenerated excitons were collected prior to recombination, $\alpha$ should be equal to 1; otherwise, the fact that $\alpha < 1$ indicates the existence to a certain extent of bimolecular charge recombination.[49] As shown in Fig. 3d, the $\alpha$ values for PBT1-C:IT-2F, PBT1-C:TTPT-T-2F, and PBT1-C:T-TPT-T-2F blends were measured to be 0.973, 0.974, and 0.979, respectively. These results indicate that negligible bimolecular recombination existed in all three nonfullerene SMA-based devices under short-circuit conditions.[50]

Atomic force microscopy (AFM) and transmission electron microscopy (TEM) were performed to investigate the morphology of all three nonfullerene SMA-based blend films. The AFM phase images for the three SMA-based blend films under different post-treatment conditions are shown in Fig. S7.† AFM and TEM images under optimal conditions are shown in Fig. 4. In terms of the PBT1-C:TTPT-T-2F film, compared with the as-cast film, the addition of DIO from 0.25% to 1% has less influence on the morphology as a clear interpenetrating fibril network morphology can be found for all the films. And the device based on the PBT1-C:TTPT-T-2F film with 0.5% DIO shows a relatively high PCE of 10.86%. After thermal annealing at 100 °C for 10 min, clear interpenetrating fibril-like network channels with an increasing fibril diameter were observed in the AFM phase image. And the corresponding device showed a high PCE of 12.71%. In contrast, upon addition of DIO into PBT1-C:IT-2F and PBT1-C:T-TPT-T-2F, both blend films exhibited excessive phase separation with overlarge aggregation phases compared to their corresponding as-cast blend films, which is unfavorable for charge transport, well consistent with the change of the photovoltaic performance. For the optimal blend films after appropriate thermal annealing (Fig. 4), clear and more robust fibril-like interpenetrating network channels were formed, which should be responsible for efficient charge separation and transport.[51] TEM images also showed uniformly distributed donor/acceptor phases and appropriate phase separation sizes favorable to exciton splitting, thus resembling the AFM images.

Grazing incident wide-angle X-ray scattering (GIWAXS) measurements were employed to investigate the behavior of molecular packing and crystallinity for the neat acceptors and blend films. The corresponding two-dimensional scattering patterns and line-cuts are displayed in Fig. 5. All three nonfullerene SMAs in neat films preferred to adopt a face-on orientation with strong (100) scattering in the in-plane (IP) direction and a distinct (010) scattering peak in the out-of-plane (OOP) direction. Moreover, the scattering intensity of the (010) π–π stacking peak in the OOP direction gradually increased from IT-2F to TTPT-T-2F and to T-TPT-T-2F, suggesting that the molecular packing is gradually enhanced, which is desirable for efficient charge transport and coincides with the variation trend of electron mobilities of pristine films. As shown in Fig. S8,† PBT1-C exhibited a sharp (100) lamellar stacking peak in the IP direction and a well-defined (010) π–π stacking peak in the OOP direction, suggesting a dominant face-on orientation. After PBT1-C was blended with the three nonfullerene SMAs, the preferable face-on orientation, which is beneficial for vertical charge transport, was still maintained in all the blend films. Nevertheless, compared to the relatively higher miscibility between two nonfullerene SMAs (IT-2F and T-TPT-T-2F) and the donor PBT1-C, the lower miscibility between TTPT-T-2F and PBT1-C enabled TTPT-T-2F-based blend films to have the strongest peak intensity of the (010) π–π stacking and the tightest π–π stacking, along with the smallest *d*-spacing of 3.66 Å in the OOP direction (see *d*-spacing for PBT1-C:IT-2F (3.85 Å) and PBT1-C:T-TPT-T-2F (3.75 Å)). This should facilitate charge

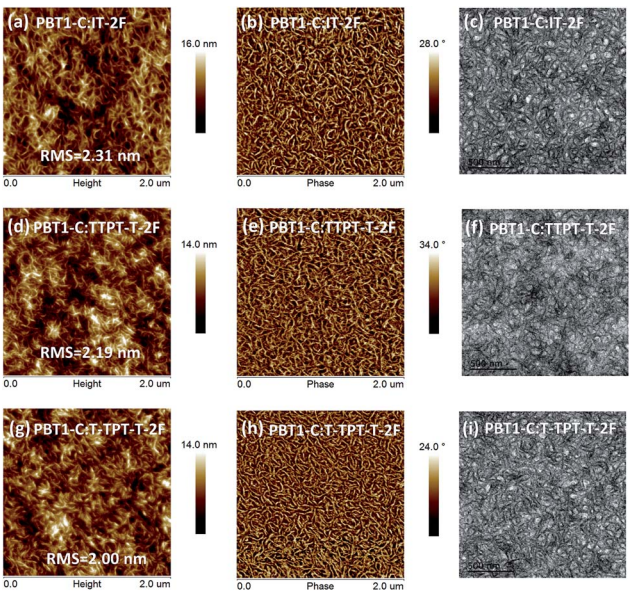


Fig. 4 AFM height and phase and TEM images: (a–c) PBT1-C:IT-2F, (d–f) PBT1-C:TTPT-T-2F, and (g–i) PBT1-C:T-TPT-T-2F blend films.

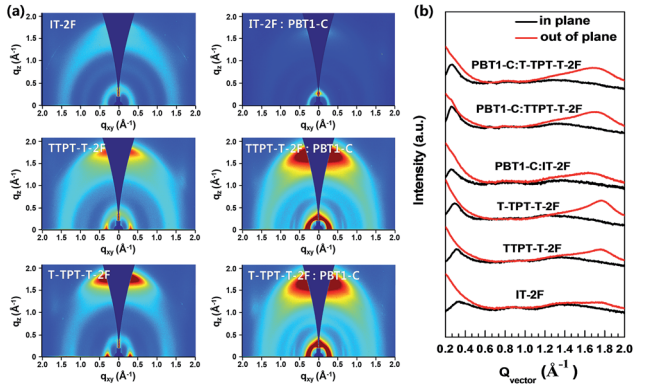


Fig. 5 (a) 2D GIWAXS patterns and (b) corresponding line-cut profiles of in-plane and out-of-plane scattering for IT-2F, TTPT-T-2F, and T-TPT-T-2F and their corresponding blend films.

transport in the vertical direction and is consistent with the SCLC measurement results.

## Conclusions

By applying a molecular cutting strategy to the IDTT skeleton, we designed and synthesized an asymmetric nonfullerene SMA, TTPT-T-2F, with an A–D–π–A structure. Compared to OSCs based on the nonfullerene SMAs IT-2F and T-TPT-T-2F featuring A–D–A and A–π–D–π–A structures, respectively, TTPT-T-2F-based OSCs showed the highest PCE of 12.71% with a $V_{oc}$ of 0.915 V, a $J_{sc}$ of 18.50 mA cm$^{-2}$, and a FF of 75.1%. The better photovoltaic performance of TTPT-T-2F-based OSCs was mainly attributed to the favorable phase separation toward efficient and more balanced charge transport in the PBT1-C:TTPT-T-2F blend. The results indicate that nonfullerene SMAs with an A–D–π–A structure are a promising class of small molecule acceptors that can be used to realize high-performance OSCs.

## Conflicts of interest

There are no conflicts to declare.

## Acknowledgements

This work was financially supported by the National Natural Science Foundation of China (NSFC) (Grant No. 21734001, 21674007, and 51825301). HYW is grateful for the financial support from the National Research Foundation (NRF) of Korea (2012M3A6A7055540 and 2015M1A2A2057506).

## Notes and references

1 Y. J. Cheng, S. H. Yang and C. S. Hsu, *Chem. Rev.*, 2009, **109**, 5868–5923.
2 Y. Li, *Acc. Chem. Res.*, 2012, **45**, 723–733.
3 J. Roncali, P. Leriche and P. Blanchard, *Adv. Mater.*, 2014, **26**, 3821–3838.
4 H. Fu, Z. Wang and Y. Sun, *Angew. Chem., Int. Ed.*, 2019, **58**, 4442–4453.
5 L. Gang, Z. Rui and Y. Yang, *Nat. Photonics*, 2012, **6**, 153–161.
6 L. Tao and T. Alessandro, *Adv. Mater.*, 2013, **25**, 1038–1041.
7 C. Yan, S. Barlow, Z. Wang, H. Yan, A. K. Y. Jen, S. R. Marder and X. Zhan, *Nat. Rev. Mater.*, 2018, **3**, 18003.
8 C. J. Brabec, S. Gowrisanker, J. J. M. Halls, D. Laird, S. Jia and S. P. Williams, *Adv. Mater.*, 2010, **22**, 3839–3856.
9 A. Distler, T. Sauermann, H. J. Egelhaaf, S. Rodman, D. Waller, K. S. Cheon, M. Lee and D. M. Guldi, *Adv. Energy Mater.*, 2014, **4**, 1300693.
10 C. B. Nielsen, S. Holliday, H. Y. Chen, S. J. Cryer and I. McCulloch, *Acc. Chem. Res.*, 2015, **48**, 2803–2812.
11 G. Zhang, J. Zhao, P. C. Y. Chow, K. Jiang, J. Zhang, Z. Zhu, J. Zhang, F. Huang and H. Yan, *Chem. Rev.*, 2018, **118**, 3447–3507.
12 C. Li, H. Fu, T. Xia and Y. Sun, *Adv. Energy Mater.*, 2019, **9**, 1900999.
13 Y. Cui, H. Yao, L. Hong, T. Zhang, Y. Xu, K. Xian, B. Gao, J. Qin, J. Zhang, Z. Wei and J. Hou, *Adv. Mater.*, 2019, **31**, 1808356.
14 J. Yuan, Y. Zhang, L. Zhou, G. Zhang, H.-L. Yip, T.-K. Lau, X. Lu, C. Zhu, H. Peng, P. A. Johnson, M. Leclerc, Y. Cao, J. Ulanski, Y. Li and Y. Zou, *Joule*, 2019, **3**, 1140–1151.
15 D. He, F. Zhao, L. Jiang and C. Wang, *J. Mater. Chem. A*, 2018, **6**, 8839–8854.
16 Z. Fei, F. D. Eisner, X. Jiao, M. Azzouzi, J. A. Rohr, Y. Han, M. Shahid, A. S. R. Chesman, C. D. Easton, C. R. McNeill, T. D. Anthopoulos, J. Nelson and M. Heeney, *Adv. Mater.*, 2018, **30**, 1705209.
17 T. Li, S. Dai, Z. Ke, L. Yang, J. Wang, C. Yan, W. Ma and X. Zhan, *Adv. Mater.*, 2018, **30**, 1705969.
18 Z. Xiao, X. Jia, D. Li, S. Wang, X. Geng, F. Liu, J. Chen, S. Yang, T. P. Russell and L. Ding, *Sci. Bull.*, 2017, **62**, 1494–1496.
19 C. Li, T. Xia, J. Song, H. Fu, H. S. Ryu, K. Weng, L. Ye, H. Y. Woo and Y. Sun, *J. Mater. Chem. A*, 2019, **7**, 1435–1441.
20 J. Song, C. Li, L. Ye, C. Koh, Y. Cai, D. Wei, H. Y. Woo and Y. Sun, *J. Mater. Chem. A*, 2018, **6**, 18847–18852.
21 C. Li, J. Song, L. Ye, C. Koh, K. Weng, H. Fu, Y. Cai, Y. Xie, D. Wei, H. Y. Woo and Y. Sun, *Sol. RRL*, 2019, **3**, 1800246.
22 Y. Yang, Z. G. Zhang, H. Bin, S. Chen, L. Gao, L. Xue, C. Yang and Y. Li, *J. Am. Chem. Soc.*, 2016, **138**, 15011–15018.
23 Y. Lin, F. Zhao, Q. He, L. Huo, Y. Wu, T. C. Parker, W. Ma, Y. Sun, C. Wang, D. Zhu, A. J. Heeger, S. R. Marder and X. Zhan, *J. Am. Chem. Soc.*, 2016, **138**, 4955–4961.
24 J. Wang, W. Wang, X. Wang, Y. Wu, Q. Zhang, C. Yan, W. Ma, W. You and X. Zhan, *Adv. Mater.*, 2017, **29**, 1702125.
25 S. Li, L. Ye, W. Zhao, S. Zhang, S. Mukherjee, H. Ade and J. Hou, *Adv. Mater.*, 2016, **28**, 9423–9429.
26 S. Dai, F. Zhao, Q. Zhang, T. K. Lau, T. Li, K. Liu, Q. Ling, C. Wang, X. Lu, W. You and X. Zhan, *J. Am. Chem. Soc.*, 2017, **139**, 1336–1343.
27 F. Zhao, S. Dai, Y. Wu, Q. Zhang, J. Wang, L. Jiang, Q. Ling, Z. Wei, W. Ma, W. You, C. Wang and X. Zhan, *Adv. Mater.*, 2017, **29**, 1700144.
28 D. Xie, T. Liu, W. Gao, C. Zhong, L. Huo, Z. Luo, K. Wu, W. Xiong, F. Liu, Y. Sun and C. Yang, *Sol. RRL*, 2017, **1**, 1700044.
29 W. Zhao, S. Li, H. Yao, S. Zhang, Y. Zhang, B. Yang and J. Hou, *J. Am. Chem. Soc.*, 2017, **139**, 7148–7151.
30 L. Ye, Y. Xie, Y. Xiao, J. Song, C. Li, H. Fu, K. Weng, X. Lu, S. Tan and Y. Sun, *J. Mater. Chem. A*, 2019, **7**, 8055–8060.
31 Y. Liu, Z. Zhang, S. Feng, M. Li, L. Wu, R. Hou, X. Xu, X. Chen and Z. Bo, *J. Am. Chem. Soc.*, 2017, **139**, 3356–3359.
32 H. Yao, Y. Cui, R. Yu, B. Gao, H. Zhang and J. Hou, *Angew. Chem., Int. Ed.*, 2017, **56**, 3045–3049.
33 F. Liu, Z. Zhou, C. Zhang, J. Zhang, Q. Hu, T. Vergote, F. Liu, T. P. Russell and X. Zhu, *Adv. Mater.*, 2017, **29**, 1606574.
34 W. Gao, M. Zhang, T. Liu, R. Ming, Q. S. An, K. Wu, D. Xie, Z. H. Luo, C. Zhong, F. Liu, F. J. Zhang, H. Yan and C. L. Yang, *Adv. Mater.*, 2018, **30**, 1800052.
35 C. Li, Y. Xie, B. Fan, G. Han, Y. Yi and Y. M. Sun, *J. Mater. Chem. C*, 2018, **6**, 4873–4877.

36 C. Li, J. Song, Y. Cai, G. Han, W. Zheng, Y. Yi, H. S. Ryu, H. Y. Woo and Y. Sun, *J. Energy Chem.*, 2020, **40**, 144–150.
37 Y. Lin, J. Wang, Z. G. Zhang, H. Bai, Y. Li, D. Zhu and X. Zhan, *Adv. Mater.*, 2015, **27**, 1170–1174.
38 T. Liu, L. Huo, S. Chandrabose, K. Chen, G. Han, F. Qi, X. Meng, D. Xie, W. Ma, Y. Yi, J. M. Hodgkiss, F. Liu, J. Wang, C. Yang and Y. Sun, *Adv. Mater.*, 2018, **30**, 1707353.
39 F. Yang, C. Li, W. Lai, A. Zhang, H. Huang and W. Li, *Mater. Chem. Front.*, 2017, **1**, 1389–1395.
40 S. Ko, E. T. Hoke, L. Pandey, S. Hong, R. Mondal, C. Risko, Y. Yi, R. Noriega, M. D. McGehee, J. L. Bredas, A. Salleo and Z. Bao, *J. Am. Chem. Soc.*, 2012, **134**, 5222–5232.
41 S. Dai, T. Li, W. Wang, Y. Xiao, T. K. Lau, Z. Li, K. Liu, X. Lu and X. Zhan, *Adv. Mater.*, 2018, **30**, 1706571.
42 H. C. Liao, C. C. Ho, C. Y. Chang, M. H. Jao, S. B. Darling and W. F. Su, *Mater. Today*, 2013, **16**, 326–336.
43 T. Xia, Y. Cai, H. Fu and Y. Sun, *Sci. China: Chem.*, 2019, **62**, 662–668.
44 J. C. Hummelen, C. J. Brabec, A. C. Cravino, D. Meissner, N. S. Sariciftci, T. Fromherz, M. T. Rispens and L. Sanchez, *Adv. Funct. Mater.*, 2010, **11**, 374–380.
45 M. C. Scharber, D. Mühlbacher, M. Koppe, P. Denk, C. Waldauf, A. J. Heeger and C. J. Brabec, *Adv. Mater.*, 2006, **18**, 789–794.
46 C. J. Brabec, A. Cravino, D. Meissner, N. S. Sariciftci, M. T. Rispens, L. Sanchez, J. C. Hummelen and T. Fromherz, *Thin Solid Films*, 2002, **403–404**, 368–372.
47 J. Comyn, *Int. J. Adhes. Adhes.*, 1992, **12**, 145–149.
48 P. W. M. Blom, V. D. Mihailetchi, L. J. A. Koster and D. E. Markov, *Adv. Mater.*, 2007, **19**, 1551–1566.
49 L. Ye, Y. Xie, K. Weng, H. S. Ryu, C. Li, Y. Cai, H. Fu, D. Wei, H. Y. Woo, S. Tan and Y. Sun, *Nano Energy*, 2019, **58**, 220–226.
50 Y. Yang, J. C Wang, H. Xu, X. W. Zhan and X. G. Chen, *ACS Appl. Mater. Interfaces*, 2018, **10**, 18984–18992.
51 Y. Xie, F. Yang, Y. Li, M. A. Uddin, P. Bi, B. Fan, Y. Cai, X. Hao, H. Y. Woo, W. Li, F. Liu and Y. Sun, *Adv. Mater.*, 2018, **30**, 1803045.